



# Properties of Titanium isotopes in complex momentum representation within relativistic mean-field theory

Tai-Hua Heng<sup>1</sup> · Yao-Wu Chu<sup>1</sup>

Received: 11 April 2022 / Revised: 24 July 2022 / Accepted: 27 July 2022 / Published online: 15 September 2022

© The Author(s), under exclusive licence to China Science Publishing & Media Ltd. (Science Press), Shanghai Institute of Applied Physics, the Chinese Academy of Sciences, Chinese Nuclear Society 2022

**Abstract** The self-consistent quadruple potential is deduced within the relativistic mean-field (RMF) framework and substituted into the Hamiltonian, which is calculated using the complex momentum representation (CMR). Considering even-even titanium isotopes as an example, this study investigated various properties, including the resonant states of neutron-rich nuclei in the RMF-CMR model, and used them to describe the binding energy. The abrupt decrease in the two-neutron separation energy ( $S_{2n}$ ) corresponds to the traditional magic number. The resonant and bound states are simultaneously exposed in the complex moment plane, where the continuum is along the integration contour. The four oblate neutron-rich nuclei  $^{72-78}\text{Ti}$  are weakly bound or resonant because their Fermi energies are approximately 0 MeV. The root-mean-square (RMS) radii of these nuclei increase suddenly compared with those of others (neutron number  $N < 48$ ). Moreover,  $^{78}\text{Ti}$  and  $^{76}\text{Ti}$  are determined as drip-line nucleons by the value of  $S_{2n}$  and the energy levels, respectively. Finally, the weak-bounded character can be represented by diffuse density probability distributions.

**Keywords** Resonant states · Self-consistent potential · Complex momentum representation

## 1 Introduction

In past decades, the location of the edge of the nuclear chart has become an important issue in nuclear physics. As is well known, the neutron-side drip line can be experimentally determined from oxygen isotopes up to  $Z = 10$  [1, 2]. Generally, nuclei that are far from the  $\beta$  stable line exhibit interesting properties, such as deformation structure [3], new magic number [4], halo [5, 6], giant halo phenomena [7], and  $\beta$  decay [8], owing to the large  $N/Z$  ratio. The halo of  $^{11}\text{Li}$  and deformed halo of  $^{31}\text{Ne}$  can be explained by simultaneously considering the continuum and resonant states. Therefore, the theory of nuclear structure is not only appropriate for investigating the bound states but also for investigating the resonant states and continuum states.

In recent years, relativistic mean-field theory has become established [9] because it successfully explains the  $\beta^+/\text{EC}$  decay [10], charge-exchange excitations [11], shell correction energies [12], nuclear mass precision [13], shape phase transitions [14, 15] of spherical and deformed nuclei, hypernuclei [16, 17], nuclear matter [18, 19], and descriptions of astrophysical  $r$ -process simulations [20, 21]. To date, several methods have been developed to study the properties of resonant states. Some of these methods, such as the  $R$ -matrix [22],  $K$ -matrix [23], and  $S$ -matrix [24, 25], are based on scattering theory. However, resonant states are dealt within a manner similar to bound states. For example, by the analytic continuation in the coupling constant (ACCC) [26] method, resonance states

---

This study was partly supported by the National Natural Science Foundation of China (Nos. 11935001 and 11875070), and Natural Science Foundation of Anhui Province (No. 1908085MA16).

---

✉ Tai-Hua Heng  
hength@ahu.edu.cn

<sup>1</sup> School of Physics and Optoelectronic Engineering, Anhui University, Hefei 230601, China

become bound states, and the physical quantities can be obtained from the bound-state solutions through the Padé approximate (PA) order. Several neutron-rich nuclei have been investigated using the ACCC method combined with relativistic mean-field (RMF) theory [27, 28]. The equation of motion in the real stabilization method (RSM) [29] can be solved based on a box of finite sizes, and the energy is stable against changes in the size of the basis or box. However, this method is not suitable for broad-width resonant states. Satisfactory results for spherical nuclei  $^{120}\text{Sn}$  have been obtained by using Green’s function (GF) to solve the density of states in coordinate space [30, 31]. The complex scaling method (CSM) [32] is used in atomic and molecular physics and nuclear physics [33, 34]. Based on the RMF-CSM method, the resonant states of spherical [35, 36] and deformed nuclei have been analyzed [37].

Although RMF-RSM, RMF-ACCC, and RMF-CSM are effective tools for dealing with resonant states, various limitations still exist, and it is difficult to obtain the resonance state near the threshold of the continuum spectrum with satisfactory accuracy. Additionally, the result calculated using the CSM method is affected by the rotation angle. Recently, because the bound and resonant states can be shown simultaneously by solving the equation of motion in complex momentum space, a scheme wherein the complex momentum representation (CMR) is applied to the RMF framework was established [38]. Using the RMF-CMR method, several quantities of the resonance states can be obtained for the spherical system [39, 40]. Additionally, the deformed nuclei characteristics have been investigated using a Woods-Saxon type potential for both nonrelativistic [41, 42] and relativistic cases [43] in a complex momentum plane. Numerous novel conclusions have been drawn for typical halo nuclei such as  $^{37}\text{Mg}$ ,  $^{31}\text{Ne}$ , and  $^{19}\text{C}$ . This study considered titanium isotopes as an example and investigated various properties using the RMF-CMR method within the self-consistent potential obtained by iteratively solving the Dirac equation in the RMF framework. The rest of this paper is organized as follows. Section 2 presents the derivation of the theoretical formulas. The numerical details and results are presented in Sect. 3. Finally, the summary and direction of future work are presented in Sect. 4.

## 2 Theoretical framework

To deduce the self-consistent potential as the starting point, the following Lagrangian of RMF theory is given:

$$\begin{aligned} \mathcal{L} = & \bar{\psi} [i\gamma^\mu \partial_\mu - M - g_\sigma \sigma - g_\omega \gamma^\mu \omega_\mu - g_\rho \gamma^\mu \vec{\tau} \cdot \vec{\rho}_\mu \\ & - e \frac{1 - \tau_3}{2} \gamma^\mu A_\mu] \psi + \frac{1}{2} \partial_\mu \sigma \partial^\mu \sigma - \frac{1}{2} m_\sigma^2 \sigma^2 \\ & - \frac{g_2}{3} \sigma^3 - \frac{g_3}{4} \sigma^4 - \frac{1}{4} \Omega_{\mu\nu} \Omega^{\mu\nu} + \frac{1}{2} m_\omega^2 \omega_\mu \omega^\mu \\ & + \frac{1}{4} c_3 (\omega_\mu \omega^\mu)^2 - \frac{1}{4} \vec{R}^{\mu\nu} \cdot \vec{R}_{\mu\nu} + \frac{1}{2} m_\rho^2 \vec{\rho}_\mu \cdot \vec{\rho}^\mu \\ & + \frac{1}{4} d_3 (\vec{\rho}_\mu \cdot \vec{\rho}^\mu)^2 - \frac{1}{4} F^{\mu\nu} F_{\mu\nu}, \end{aligned} \tag{1}$$

where  $M$  denotes the nuclear mass;  $m_\sigma(g_\sigma)$ ,  $m_\omega(g_\omega)$ , and  $m_\rho(g_\rho)$  represent the masses (coupling constants) of the respective mesons;  $g_2$ ,  $g_3$ ,  $c_3$ , and  $d_3$  are self-coupling coefficients.

The corresponding Dirac equation in cylindrical coordinates is used to investigate the characteristics of the deformed nuclei and is expressed as follows:

$$(\vec{\alpha} \cdot \vec{p} + \beta(M + S) + V)\Psi = \epsilon\Psi. \tag{2}$$

where  $\vec{\alpha}$  and  $\beta$  are Dirac matrices;  $S$  and  $V$  are the scalar and vector potential, respectively. The solution of this equation includes the bound states and continuum with the following complete condition:

$$\sum_b^{N_b} |\Psi_b\rangle \langle \Psi_b| + \int d\epsilon_c |\Psi_c\rangle \langle \Psi_c| = 1, \tag{3}$$

where  $\Psi_b$  and  $\Psi_c$  are the wave functions of the bound states and continuum, respectively.

Several methods, such as the shooting method [44] and finite element method [45], have been developed to solve the Dirac equation. Notably, spurious states can be completely avoided because the Dirac equation is considered within momentum space. To investigate the resonant states submerged in the continuum, the Dirac equation must be converted into the following complex momentum plane:

$$\int d\vec{k}' (\vec{k}' | H | \vec{k}) \psi(\vec{k}') = \epsilon \psi(\vec{k}), \tag{4}$$

with the wave vector  $\vec{k} = \vec{p}/\hbar$ . The wave function is divided into radial and angular parts:

$$\begin{aligned} \psi(\vec{k}) = & \psi_{m_j}(\vec{k}) \\ = & \sum_{ij} \begin{pmatrix} f^{ij}(k) \phi_{ijm_j}(\Omega_k) \\ g^{ij}(k) \phi_{\bar{i}j m_j}(\Omega_k) \end{pmatrix}, \end{aligned} \tag{5}$$

where  $\bar{l} = 2j - l$ . The former  $f$  and  $g$  are the radial components, and the angular part is expressed as follows:

$$\phi_{ijm_j}(\Omega_k) = \sum_{m_s} \langle lm \frac{1}{2} m_s | jm_j \rangle Y_{lm}(\Omega_k) \chi_{m_s}, \tag{6}$$

Here,  $\chi_{m_s}$  is the spin wave function with the third component of the spin angular momentum  $m_s$ , and  $Y_{lm}(\Omega_k)$  denotes the spherical harmonics in complex momentum space.

By substituting Eq. (5) into Eq. (4), the Dirac equation becomes as follows:

$$\begin{cases} Mf^{lj}(k) - kg^{lj}(k) + \sum_{l'j'} \int k'^2 dk' V^+(l', j', p, q, l, j, m_j, k, k') f^{l'j'}(k') = \epsilon f^{lj}(k), \\ -kf^{lj}(k) - Mg^{lj}(k) + \sum_{l'j'} \int k'^2 dk' V^-(l', j', p, q, l, j, m_j, k, k') g^{l'j'}(k') = \epsilon g^{lj}(k), \end{cases} \quad (7)$$

where  $V^+$  and  $V^-$  are expressed as follows:

$$\begin{aligned} V^+(l', j', p, q, l, j, m_j, k, k') &= (-)^{l+l'} \frac{2}{\pi} \int r^2 dr [V(r) + S(r)] j_l(kr) j_{l'}(k'r) \\ &\quad \sum_{m_s} \langle lm | Y_{pq}(\Omega_r) | l'm' \rangle \langle lm \frac{1}{2} m_s | j m_j \rangle \langle l'm' \frac{1}{2} m_s | j' m_j \rangle, \\ V^-(\tilde{l}, \tilde{j}', p, q, \tilde{l}, \tilde{j}, m_j, k, k') &= (-)^{\tilde{l}+\tilde{l}'} \frac{2}{\pi} \int r^2 dr [V(r) - S(r)] j_{\tilde{l}}(kr) j_{\tilde{l}'}(k'r) \\ &\quad \sum_{m_s} \langle \tilde{l}\tilde{m} | Y_{pq}(\Omega_r) | \tilde{l}\tilde{m}' \rangle \langle \tilde{l}\tilde{m} \frac{1}{2} m_s | j m_j \rangle \langle \tilde{l}\tilde{m}' \frac{1}{2} m_s | j' m_j \rangle. \end{aligned} \quad (8)$$

To simplify the calculations, this study adopted the Gauss-Legendre approximation. Accordingly, the following transformations can be carried out:  $\mathbf{f}(k_a) = \sqrt{w_a} k_a f(k_a)$  and  $\mathbf{g}(k_a) = \sqrt{w_a} k_a g(k_a)$ , where  $k_a$  is the grid point of the Gauss-Legendre quadrature. The corresponding mesh point number (ngl) in the CMR code is 60. The same number (60) is also set for the grid point of the Gauss Hermite quadrature (ngh) in the coordinate space of the RMF framework. Thus, the Dirac equation becomes a symmetric matrix equation, as follows:

$$\begin{cases} \sum_b [M\delta_{ab} \mathbf{f}^b(k_b) + \sum_{l'j'} \sqrt{w_a w_b} k_a k_b V^+(l', j', p, q, l, j, m_j, k_a, k_b) \mathbf{f}^{l'j'}(k_b) - k_a \delta_{ab} \mathbf{g}^b(k_b)] = \epsilon \mathbf{f}^a(k_a), \\ \sum_b [-k_a \delta_{ab} \mathbf{f}^b(k_b) - M\delta_{ab} \mathbf{g}^b(k_b) + \sum_{l'j'} \sqrt{w_a w_b} k_a k_b V^-(l', j', p, q, l, j, m_j, k_a, k_b) \mathbf{g}^{l'j'}(k_b)] = \epsilon \mathbf{g}^a(k_a). \end{cases} \quad (9)$$

At this point, the Dirac equation can be treated by solving the eigenvalue of a symmetric matrix in Eq. (9). More details regarding this formulation can be found in the literature [41, 43].

### 3 Numerical details and results

Based on the above-mentioned theoretical formula, various properties of Ti isotopes, such as the binding energy, single-particle energy level,  $S_{2n}$ , RMS radius, and

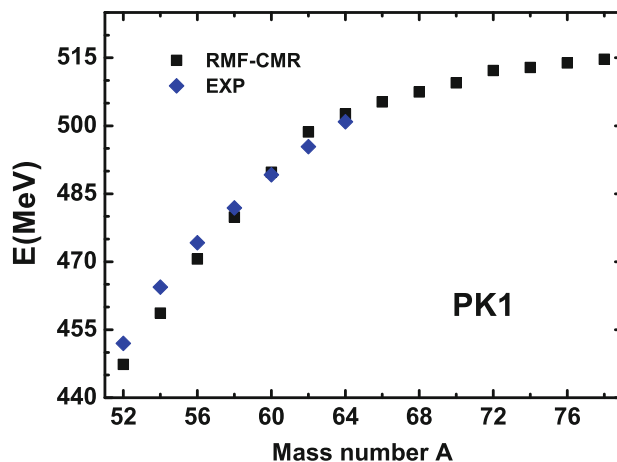
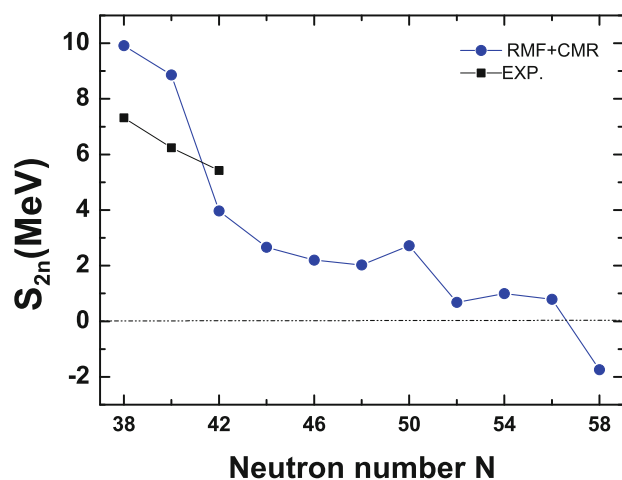


Fig. 1 (Color online) Binding energies as function of mass number. The blue diamonds represent the data in AME2020. The black squares represent the values calculated using RMF-CMR model

probability distribution, can be investigated. To study the characteristics of resonant states, the neutron number of the Ti isotopes is considered to be up to 56 ( $^{78}\text{Ti}$ ). In this calculation, the coupled-channel model is adopted and the PK1 parameter group is selected. The number of coupling channels (nch) is equal to four. The infinite complex momentum plane is truncated at  $\text{Re } k = 4.0 \text{ fm}^{-1}$ , which is sufficient for the convergence of the numerical computation.

Figure 1 shows the calculated binding energy as a function of the mass number. For comparison, the related data from AME2020 [46] are also indicated by blue diamonds. The results of the experimental data are almost in agreement, which validates the calculations carried out by this study. Therefore, the RMF-CMR model can be successfully used to describe the stable nuclei among the Ti isotopes, and the pro model is valid for investigating other properties of neutron-rich nuclei, even close to the drip line. Moreover, the binding energy increases slowly as the neutron number increases, which means that the nucleon becomes increasingly softer.

The two-neutron separation energy  $S_{2n}$  is a physical quality in nuclear physics and is used for investigating the shell structure of a nucleon, as shown in Fig. 2. As is well known, the drip-line nucleon can be predicted by the value of  $S_{2n}$ . As shown in Fig. 2,  $S_{2n}$  gradually decreases as the number of neutrons increases. Specifically, the value of  $S_{2n}$  decreases abruptly when the neutron number  $N = 40$ , which corresponds to the subshell. Notably, the shell gap is not obvious in  $^{72}\text{Ti}$  with the traditional magic number  $N = 50$ . Therefore, it is considered that the large  $N/Z$  ratio is the main contributor. Additionally, it is shown that  $S_{2n}$  is close to the zero-scale line when  $N > 50$ . The value of  $S_{2n}$  is less than 0 MeV when  $N = 58$ . Hence,  $^{78}\text{Ti}$  is predicted



**Fig. 2** (Color online) The two-neutron separation energies ( $S_{2n}$ ) with the RMF+CMR model are indicated by a blue circle as a function of the neutron number  $N$ . For comparison, the experimental data are also indicated by a black square.[46]

to be the drip-line nucleon for the Ti isotopes. However, some experimental data do not support the shell structure, because the neutron number is equal to 40. For  $^{60-64}\text{Ti}$ , the  $S_{2n}$  values are significantly different to those of the RMF+CMR model. The three sets of experimental data exhibit linear decrease. The two former values are lower by more than 2 MeV compared with the theoretical calculation, and the last value is larger by 1.45 MeV. With the development of the radioactive isotope beam factory, isotones around neutron number 40 were first observed in 2020 [47, 48]. The experimental results revealed a deformed  $^{62}\text{Ti}$  ground state. The Jahn-Teller effect is related to the increase in the two-neutron separation energies in the vicinity of  $^{62}\text{Ti}$ . The large-scale shell model calculation reproduced the present measurement and disfavored the doubly-magic character of  $^{60}\text{Ca}$ .

The single-particle spectrum is an important property for describing nuclear structures. In accordance with the CMR method reported in [41, 43], this study tested different contours, and the same momentum integration contour was selected for all Ti isotope nuclei. The selected contour is a triangular contour with the four key points  $k = 0 \text{ fm}^{-1}$ ,  $k = 0.4 - i0.4 \text{ fm}^{-1}$ ,  $k = 0.8 \text{ fm}^{-1}$ , and  $k_{\text{max}} = 4.0 \text{ fm}^{-1}$ . To show the resonance states clearly in the triangular contour, the real axis  $\text{Re } k$  and imaginary axis  $\text{Im } k$  are truncated to  $1.2 \text{ fm}^{-1}$  and  $0.4 \text{ fm}^{-1}$ , respectively.

Figure 3 shows various eigenstates of  $^{72-78}\text{Ti}$  in the complex momentum plane, corresponding to  $\frac{1}{2}^+$ ,  $\frac{5}{2}^+$ ,  $\frac{3}{2}^+$ , and  $\frac{1}{2}^+$ , respectively. The black diamonds indicate the negative-energy bound states on the vertical axis, owing to the mass-energy relationship. The blue circles indicate the continuum located on the contour. The red triangles indicate the

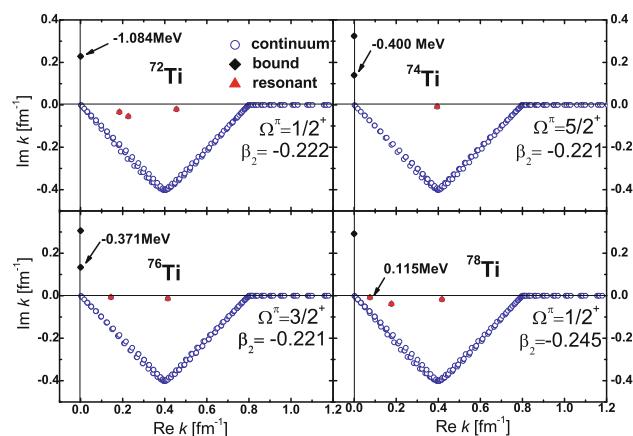


**Fig. 3** (Color online) The single-particle spectra in  $^{72-78}\text{Ti}$  for the states occupied by the last neutron are presented in the complex momentum plane. The blue circle, black diamond, and brown triangle represent the continuum, bound states, and resonant states, respectively

positions of the resonant states located in the fourth quadrant of the complex momentum plane. Owing to the deformed shape, the self-consistent potential is applied to obtain the quadrupole deformation parameter ( $\beta_2$ ) tagged in this figure. Owing to the negative deformation values, the four neutron-rich nuclei are oblate.

Although not all bound states are drawn, the eigenstates occupied by the last neutron are presented, and their eigenenergies indicate that the last neutrons in  $^{72-76}\text{Ti}$  are weakly bounded; therefore, these nuclei become increasingly softer as the number of neutrons increases. As can be seen, the energy level related to  $^{78}\text{Ti}$  is positive, and the relevant width of 0.052 MeV can be obtained, which means that the last neutron is resonant and  $^{78}\text{Ti}$  should not exist stably. As shown in Fig. 2, this study predicted that the drip-line nucleon of Ti is  $^{78}\text{Ti}$ . The results of the two assessments are different but very similar.

To better investigate the exotic structure of the even-even neutron-rich titanium isotopes, the single-particle levels of all nuclei ( $38 \leq N \leq 56$ ) are shown in Fig. 4 and are indicated by different colors. The quantum number of the last neutron of each Ti nucleus is also marked in the figure. The shell gap (3.562 MeV) of  $^{62}\text{Ti}$  between levels  $1/2[301]$  and  $9/2[404]$  is more significant than that of the adjacent nuclei supporting the subshell structure ( $N = 40$ ). This result is consistent with the description of the two-neutron separation energy. Additionally, the quadrupole deformation  $\beta_2$  indicates the spherical structure of  $^{62}\text{Ti}$ . For  $^{60-70}\text{Ti}$ , the energy levels occupied by the last neutron increase with the isospin. However, the highest energy is lower than 0 MeV; therefore, these nuclei remain bound. With the further increase in the neutron number, the shell structure of  $^{72}\text{Ti}$  is considered. Notably, a large shell gap

does not exist between the  $1/2 [440]$  and  $5/2 [413]$  levels compared with that of  $^{72}\text{Ti}$ . Hence, the traditional magic number ( $N = 50$ ) is not clearly shown. For  $^{74}\text{Ti}$  and  $^{76}\text{Ti}$ , the Fermi level is  $-0.400$  MeV and  $-0.371$  MeV, respectively. Therefore, these two nuclei are weakly bound. Moreover, the  $5/2[413]$ ,  $3/2[422]$ , and  $1/2[431]$  levels occupied the last neutron of  $^{74-78}\text{Ti}$ , and these levels correspond to the  $2d_{5/2}$  level.

The nuclear radius is also an important parameter for investigating the characteristics of exotic nuclei. Figure 5

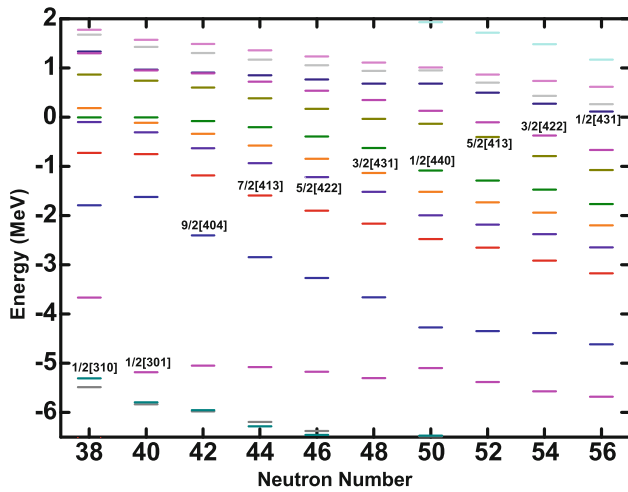


**Fig. 4** (Color online) Energy levels as function of neutron numbers of Ti isotopes. For each nucleus, the energy level of the last neutron is indicated by the quantum number

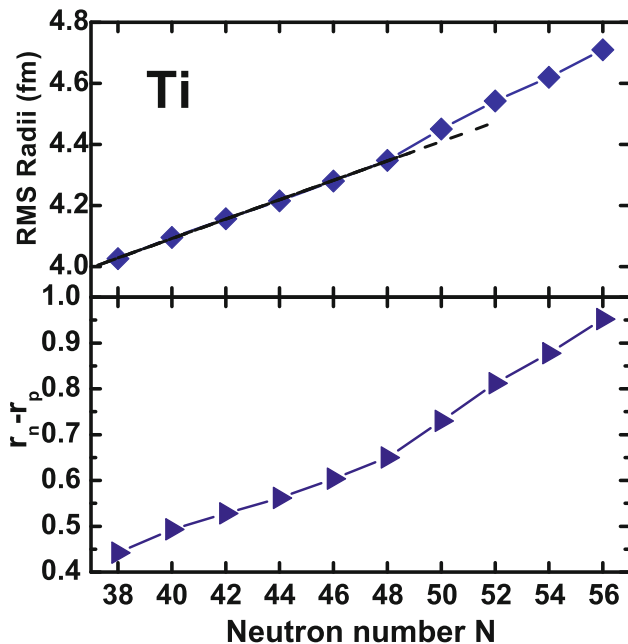


**Fig. 5** (Color online) Neutron RMS radii and radii difference of neutron and proton as function of neutron numbers of Titanium isotopes

shows the neutron RMS radii and the difference in the radii between the neutron and proton of titanium isotopes. As can be clearly seen, the neutron RMS radius increases monotonously with the isospin. According to the calculated data, a fitted dashed line is drawn in the top panel when the neutron number ranges from  $N = 38$  to  $N = 48$ . The neutron RMS radius is approximately linear. However, for neutron-rich nuclei ( $50 \leq N \leq 56$ ), the data points of the neutron RMS radii are above the dashed line and further away.

The radii differences between the neutrons and protons are shown in the bottom panel. Similar to the neutron RMS radii, when the neutron number  $N$  is greater than 48, the properties of the neutron skin are determined by a rapid increase in the differences. Notably,  $^{72}\text{Ti}$  is neutron-rich and exhibits a certain exotic character, although its magic number is 50. Thus, several novel points can be observed with regard to  $S_{2n}$  and the radius. The radius increase in  $^{72}\text{Ti}$  is attributed to the last energy level  $1/2[440]$ , where the radial density is slightly diffuse. Hence, the neutron skin phenomenon is particularly evident in  $^{70-78}\text{Ti}$ .

The exotic phenomenon is reflected by the energy levels and RMS radius and is also illustrated by the diffuse spatial distribution. According to the wave functions obtained from the Dirac equation, the radial momentum probability distribution (RMPD) is shown for several states, including those occupied by the last neutron of  $^{72-78}\text{Ti}$  in Fig. 6. To clarify the RMPD, the horizontal axis is cut at  $\text{Re } k = 2 \text{ fm}^{-1}$  and the RMPD vanishes when  $\text{Re } k$  is more than  $2 \text{ fm}^{-1}$ . Different single-particle levels are indicated by different colors. The density distributions of the last neutron and the other neutrons are expressed by solid and dashed lines, respectively. The background of the continuum is not shown in the figure. As can be seen, all states expand

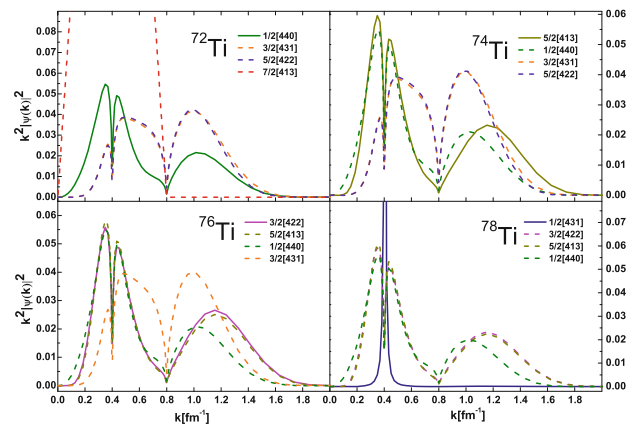


**Fig. 6** (Color online) Radial-momentum density distribution for several states of  $^{72-78}\text{Ti}$ . The solid and dashed lines indicate the eigenstates occupied by the last neutron and the other neutrons, respectively

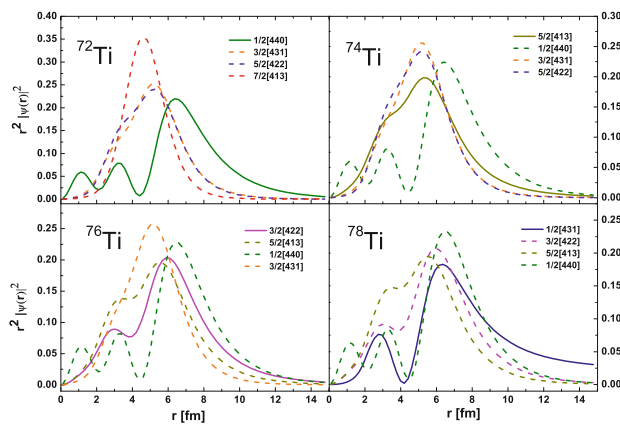


**Fig. 7** (Color online) Radial density distribution in coordinate representation. The solid lines indicate the eigenstates occupied by the last neutron; the dashed lines indicate states with a lower energy level

widely with an increase in momentum. In this figure, the blue solid line is the  $\delta$  function, which gives the eigenstate occupied by the last neutron in  $^{78}\text{Ti}$ . In complex momentum space, the radial momentum probability distributions for both the resonant states and bound states converge.

The density distribution in the coordinate representation, after the wave functions are transformed into a coordinate plane, is also considered. In Fig. 7, the radial density distribution for  $^{72-78}\text{Ti}$  is shown as a function of coordinate  $r$ . Similar to Fig. 6, the different colors indicate different energy levels. The solid lines represent the eigenstates occupied by the last neutrons of the four nuclei. The three dashed lines in each panel indicate other lower levels. Obviously, almost all lines decrease to zero at the edge of the box ( $r = 15$  fm). However, the blue solid line for the density distribution of eigenstate  $1/2[431]$  of  $^{78}\text{Ti}$  does not converge at the border, which matches the characteristics of the resonant states. By combining the energy values shown in Fig. 4, the diffuse density distribution confirms that  $^{78}\text{Ti}$  is not a stable nucleus. Therefore,  $^{76}\text{Ti}$  is the last stable nucleus in the Ti isotopic chain.

## 4 Summary and prospective

This study investigated even-even titanium isotopes using the RMF-CMR method. The deformed self-consistent potential was derived within the RMF framework and was then used to investigate the resonant states in the CMR model. First, the binding energies of  $^{52-64}\text{Ti}$  are in good agreement with the data in AME2020. The  $S_{2n}$  value obtained from the binding energy reproduced the magic number  $N = 40$ . However, the traditional magic number  $N = 50$  shell gap is not obvious. Moreover, the value of  $S_{2n}$  predicts that  $^{78}\text{Ti}$  is a drip-line nucleus for Ti isotopes. In

the complex momentum plane, the bound states and resonant states are displayed and distinguished from the continuum. A subshell structure ( $N = 40$ ) is observed in  $^{62}\text{Ti}$  based on the large energy gap, and the traditional magic number ( $N = 50$ ) disappears owing to the large  $N/Z$  ratio in  $^{72}\text{Ti}$ . The shape of  $^{62}\text{Ti}$  is approximately spherical, and  $^{72-78}\text{Ti}$  is obviously deformed. The RMS radii of  $^{60-70}\text{Ti}$  increase linearly, whereas the RMS radii of  $^{72-78}\text{Ti}$  increase abruptly. These energy levels and the RMS radii indicate that  $^{72-76}\text{Ti}$  is weakly bound, while  $^{78}\text{Ti}$  is resonant. Finally, the radial density distributions in the complex momentum plane and coordinate space were presented based on the calculated wave functions. The radial distribution of the resonant states in  $^{78}\text{Ti}$  in the coordinate representation is slightly diffuse. Based on these two assessment criteria, this study predicted that the drip-line nucleus of the Ti isotope is  $^{78}\text{Ti}$  or  $^{76}\text{Ti}$ .

Satisfactory results were obtained for the titanium isotopic chain using the RMF-CMR method, and this is the first time that the resonant state has been investigated using the CMR model and self-consistent potential. The development of a CMR model is important, and future work will consider the pairing correlation in this theoretical formalism. Tensor interactions [49] or Jahn-Teller effects may also help in elucidating the experimental phenomena and the edge of the nuclear chart.

**Author Contributions** All authors contributed to the study conception and design. Material preparation, data collection and analysis were performed by Tai-Hua Heng and Yao-Wu Chu. The first draft of the manuscript was written by Tai-Hua Heng and all authors commented on previous versions of the manuscript. All authors read and approved the final manuscript.

## References

1. D.S. Ahn, N. Fukuda, H. Geissel et al., Location of the neutron dripline at fluorine and neon. *Phys. Rev. Lett.* **123**, 212501 (2019). <https://doi.org/10.1103/PhysRevLett.123.212501>
2. H. Sakurai, S.M. Lukyanov, M. Notani et al., Evidence for particle stability of  $^{31}\text{F}$  and particle instability of  $^{25}\text{N}$  and  $^{28}\text{O}$ . *Phys. Lett. B.* **448**, 180 (1999). [https://doi.org/10.1016/S0370-2693\(99\)00015-5](https://doi.org/10.1016/S0370-2693(99)00015-5)
3. I. Tanihata, H. Hamagaki, O. Hashimoto et al., Measurements of interaction cross sections and nuclear radii in the light p-shell region. *Phys. Rev. Lett.* **55**, 2676 (1985). <https://doi.org/10.1103/PhysRevLett.55.2676>
4. A. Ozawa, T. Kobayashi, T. Suzuki et al., New magic number,  $N = 16$ , near the Neutron Drip Line. *Phys. Rev. Lett.* **84**, 5493 (2000). <https://doi.org/10.1103/PhysRevLett.84.5493>
5. S.S. Zhang, S.Y. Zhong, B. Shao et al., Self-consistent description of the halo nature of  $^{31}\text{Ne}$  with continuum and pairing correlations. *J. Phys. G: Nucl. Part. Phys.* **49**, 025102 (2022). <https://doi.org/10.1088/1361-6471/ac430e>
6. S.Y. Zhong, S.S. Zhang, X.X. Sun et al., Study of the deformed halo nucleus  $^{31}\text{Ne}$  with Glauber model based on microscopic self-

- consistent structures. *Sci. China-Phys. Mech. Astron.* **65**, 262011 (2022). <https://doi.org/10.1007/s11433-022-1894-6>
7. Y. Zhang, M. Matsuo, J. Meng, Pair correlation of giant halo nuclei in continuum Skyrme-Hartree-Fock-Bogoliubov theory. *Phys. Rev. C* **86**, 054318 (2012). <https://doi.org/10.1103/PhysRevC.86.054318>
  8. D.Z. Chen, D.L. Fang, C.L. Bai, Impact of finite-range tensor terms in the Gogny force on the  $\beta$ -decay of magic nuclei. *Nucl. Sci. Tech.* **32**, 74 (2021). <https://doi.org/10.1007/s41365-021-00908-9>
  9. J. Walecka, A theory of highly condensed matter. *Ann. Phys. (N.Y.)* **83**, 491 (1974). [https://doi.org/10.1016/0003-4916\(74\)90208-5](https://doi.org/10.1016/0003-4916(74)90208-5)
  10. Z.M. Niu, Y.F. Niu, Q. Liu et al., Nuclear  $\beta$ +EC decays in covariant density functional theory and the impact of isoscalar proton-neutron pairing. *Phys. Rev. C* **87**, 051303(R) (2013). <https://doi.org/10.1103/PhysRevC.87.051303>
  11. Z.M. Niu, Y.F. Niu, H.Z. Liang et al., Self-consistent relativistic quasiparticle random-phase approximation and its applications to charge-exchange excitations. *Phys. Rev. C* **95**, 044301 (2017). <https://doi.org/10.1103/PhysRevC.95.044301>
  12. P. Jiang, Z.M. Niu, Y.F. Niu et al., Strutinsky shell correction energies in relativistic Hartree-Fock theory. comparative study of nuclear masses in the relativistic mean-field model. *Phys. Rev. C* **98**, 064323 (2018). <https://doi.org/10.1103/PhysRevC.98.064323>
  13. X.M. Hua, T.H. Heng, Z.M. Niu et al., Comparative study of nuclear masses in the relativistic mean-field model. *Sci. China: Phys. Mech. Astron.* **55**, 2414 (2012). <https://doi.org/10.1007/s11433-012-4943-y>
  14. Z.P. Li, B.Y. Song, J.M. Yao et al., Simultaneous quadrupole and octupole shape phase transitions in Thorium. *Phys. Lett. B* **726**, 866 (2013). <https://doi.org/10.1016/j.physletb.2013.09.035>
  15. Z.P. Li, T. Nikšić, D. Vretenar et al., Microscopic analysis of nuclear quantum phase transitions in the  $N \approx 90$  region. *Phys. Rev. C* **79**, 054301 (2009). <https://doi.org/10.1103/PhysRevC.79.054301>
  16. T.T. Sun, E. Hiyama, H. Sagawa et al., Mean-field approaches for  $\Xi^-$  hypernuclei and current experimental data. *Phys. Rev. C* **94**, 064319 (2016). <https://doi.org/10.1103/PhysRevC.94.064319>
  17. Z.X. Liu, C.J. Xia, W.L. Lu et al., Relativistic mean-field approach for  $\Lambda$ ,  $\Xi$ , and  $\Sigma$  hypernuclei. *Phys. Rev. C* **98**, 024316 (2018). <https://doi.org/10.1103/PhysRevC.98.024316>
  18. T.T. Sun, B.Y. Sun, J. Meng, BCS-BEC crossover in nuclear matter with the relativistic Hartree-Bogoliubov theory. *Phys. Rev. C* **86**, 014305 (2012). <https://doi.org/10.1103/PhysRevC.86.014305>
  19. T.T. Sun, S.S. Zhang, Q.L. Zhang, C.J. Xia, Strangeness and  $\Delta$  resonance in compact stars with relativistic-mean-field models. *Phys. Rev. D* **99**, 023004 (2019). <https://doi.org/10.1103/PhysRevD.99.023004>
  20. Z.M. Niu, Y.F. Niu, H.Z. Liang et al.,  $\beta$ -decay half-lives of neutron-rich nuclei and matter flow in the  $r$ -process. *Phys. Lett. B* **723**, 172 (2013). <https://doi.org/10.1016/j.physletb.2013.04.048>
  21. Z. Li, Z.M. Niu, B.H. Sun, Influence of nuclear physics inputs and astrophysical conditions on  $r$ -process. *Sci. China-Phys. Mech. Astron.* **62**, 982011 (2019). <https://doi.org/10.1007/s11433-018-9355-y>
  22. G.M. Hale, R.E. Brown, N. Jarmie, Pole structure of the  $J^\pi = 3/2^+$  resonance in  $^5\text{He}$ . *Phys. Rev. Lett.* **59**, 763 (1987). <https://doi.org/10.1103/PhysRevLett.59.763>
  23. J. Humblet, B.W. Filippone, S.E. Koonin, Level matrix,  $^{16}\text{N}\beta$  decay, and the  $^{12}\text{C}(\alpha, \gamma)^{16}\text{O}$  reaction. *Phys. Rev. C* **44**, 2530 (1991). <https://doi.org/10.1103/PhysRevC.44.2530>
  24. J.R. Taylor, *Scattering theory: the quantum theory on nonrelativistic collisions* (JohnWiley and Sons, New York, 1972). <https://doi.org/10.1063/1.3128052>
  25. Z.P. Li, J. Meng, Y. Zhang et al., Single-particle resonances in a deformed Dirac equation. *Phys. Rev. C* **81**, 034311 (2010). <https://doi.org/10.1103/PhysRevC.81.034311>
  26. V.I. Kukulin, V.M. Krasnopl'sky, J. Horáček, *Theory of resonances: principles and applications* (Kluwer Academic, Dordrecht, 1989). <https://doi.org/10.1007/978-94-015-7817-2>
  27. S.S. Zhang, J. Meng, S.G. Zhou et al., Analytic continuation of single-particle resonance energy and wave function in relativistic mean field theory. *Phys. Rev. C* **70**, 034308 (2004). <https://doi.org/10.1103/PhysRevC.70.034308>
  28. X.D. Xu, S.S. Zhang, A.J. Signoracci et al., Analytical continuation from bound to resonant states in the Dirac equation with quadrupole-deformed potentials. *Phys. Rev. C* **92**, 024324 (2015). <https://doi.org/10.1103/PhysRevC.92.024324>
  29. H.S. Taylor, A.U. Hazi, Comment on the stabilization method: variational calculation of the resonance width. *Phys. Rev. A* **14**, 2071 (1976). <https://doi.org/10.1103/PhysRevA.14.2071>
  30. T.T. Sun, W.L. Lu, L. Qian et al., Green's function method for the spin and pseudospin symmetries in the single-particle resonant states. *Phys. Rev. C* **99**, 034310 (2019). <https://doi.org/10.1103/PhysRevC.99.034310>
  31. Y.T. Wang, T.T. Sun, Searching for single-particle resonances with the Green's function method. *Nucl. Sci. Tech.* **32**, 46 (2021). <https://doi.org/10.1007/s41365-021-00884-0>
  32. N. Moiseyev, Quantum theory of resonances: calculating energies, widths and cross-sections by complex scaling. *Phys. Rep.* **302**, 212 (1998). [https://doi.org/10.1016/S0370-1573\(98\)00002-7](https://doi.org/10.1016/S0370-1573(98)00002-7)
  33. N. Michel, W. Nazarewicz, M. Pszajczak et al., Shell model in the complex energy plane. *J. Phys. G* **36**, 013101 (2009). <https://doi.org/10.1088/0954-3899/36/1/013101>
  34. T. Myo, Y. Kikuchi, H. Masui et al., Recent development of complex scaling method for many-body resonances and continua in light nuclei. *Prog. Part. Nucl. Phys.* **79**, 1–56 (2014). <https://doi.org/10.1016/j.ppnp.2014.08.001>
  35. J.Y. Guo, X.Z. Fang, P. Jiao et al., Application of the complex scaling method in relativistic mean-field theory. *Phys. Rev. C* **82**, 034318 (2010). <https://doi.org/10.1103/PhysRevC.82.034318>
  36. M. Shi, J.Y. Guo, Q. Liu et al., Relativistic extension of the complex scaled Green function method. *Phys. Rev. C* **92**, 054313 (2015). <https://doi.org/10.1103/PhysRevC.92.054313>
  37. M. Shi, Q. Liu, Z.M. Niu et al., Relativistic extension of the complex scaling method for resonant states in deformed nuclei. *Phys. Rev. C* **90**, 034319 (2014). <https://doi.org/10.1103/PhysRevC.90.034319>
  38. N. Li, M. Shi, J.Y. Guo et al., Probing resonances of the dirac equation with complex momentum representation. *Phys. Rev. Lett.* **117**, 062502 (2016). <https://doi.org/10.1103/PhysRevLett.117.062502>
  39. K.M. Ding, M. Shi, J.Y. Guo et al., Resonant-continuum relativistic mean-field plus BCS in complex momentum representation. *Phys. Rev. C* **98**, 014316 (2018). <https://doi.org/10.1103/PhysRevC.98.014316>
  40. Y.W. Chu, T.H. Heng, Exploring the halo phenomena of medium-mass nuclei having approximately  $Z=40$  with point-coupled parameters in complex momentum representations. *Chinese Phys. C* **45**, 074107 (2021). <https://doi.org/10.1088/1674-1137/abfa84>
  41. Y.J. Tian, Q. Liu, T.H. Heng et al., Research on the halo in  $^{31}\text{Ne}$  with the complex momentum representation method. *Phys. Rev. C* **95**, 064329 (2017). <https://doi.org/10.1103/PhysRevC.95.064329>
  42. X.N. Cao, Q. Liu, J.Y. Guo, Prediction of halo structure in nuclei heavier than  $^{37}\text{Mg}$  with the complex momentum representation method. *Phys. Rev. C* **99**, 014309 (2019). <https://doi.org/10.1103/PhysRevC.99.014309>
  43. Z. Fang, M. Shi, J.Y. Guo et al., Probing resonances in the Dirac equation with quadrupole-deformed potentials with the complex

- momentum representation method. *Phys. Rev. C* **95**, 024311 (2017). <https://doi.org/10.1103/PhysRevC.95.024311>
44. J. Meng, Relativistic continuum Hartree-Bogoliubov theory with both zero range and finite range Gogny forces and their application. *Nucl. Phys. A* **635**, 3 (1998). [https://doi.org/10.1016/S0375-9474\(98\)00178-X](https://doi.org/10.1016/S0375-9474(98)00178-X)
45. J.Y. Fang, S.W. Chen, T.H. Heng, Solution to the Dirac equation using the finite difference method. *Nucl. Sci. Tech.* **31**, 15 (2020). <https://doi.org/10.1007/s41365-020-0728-6>
46. M. Wang, W.J. Huang, F.G. Kondev et al., The AME 2020 atomic mass evaluation (II). Tables, graphs and references. *Chinese Physics C* **45**, 030003 (2021). <https://doi.org/10.1088/1674-1137/abddaf>
47. M.L. Cortés, W. Rodriguez, P. Doornenbal et al., Shell evolution of N=40 isotones towards  $^{60}\text{Ca}$ : First spectroscopy of  $^{62}\text{Ti}$ . *Phys. Lett. B* **800**, 135071 (2020). <https://doi.org/10.1016/j.physletb.2019.135071>
48. S. Michimasa, M. Kobayashi, Y. Kiyokawa et al., Mapping of a new deformation region around  $^{62}\text{Ti}$ . *Phys. Rev. Lett.* **125**, 122501 (2020). <https://doi.org/10.1103/PhysRevLett.125.122501>
49. D. Wu, C.L. Bai, H. Sagawa et al., Contributions of optimized tensor interactions on the binding energies of nuclei. *Nucl. Sci. Tech.* **31**, 14 (2020). <https://doi.org/10.1007/s41365-020-0727-7>

Springer Nature or its licensor holds exclusive rights to this article under a publishing agreement with the author(s) or other rightsholder(s); author self-archiving of the accepted manuscript version of this article is solely governed by the terms of such publishing agreement and applicable law.